

# Nanoscale

Accepted Manuscript



This is an *Accepted Manuscript*, which has been through the Royal Society of Chemistry peer review process and has been accepted for publication.

*Accepted Manuscripts* are published online shortly after acceptance, before technical editing, formatting and proof reading. Using this free service, authors can make their results available to the community, in citable form, before we publish the edited article. We will replace this *Accepted Manuscript* with the edited and formatted *Advance Article* as soon as it is available.

You can find more information about *Accepted Manuscripts* in the [Information for Authors](#).

Please note that technical editing may introduce minor changes to the text and/or graphics, which may alter content. The journal's standard [Terms & Conditions](#) and the [Ethical guidelines](#) still apply. In no event shall the Royal Society of Chemistry be held responsible for any errors or omissions in this *Accepted Manuscript* or any consequences arising from the use of any information it contains.

Flexible infrared detectors based on  $p$ - $n$  junctions of multi-walled carbon  
nanotubes

Zhenlong Huang,<sup>1)</sup> Min Gao,<sup>1), a)</sup> ZhuoCheng Yan,<sup>1)</sup> Taisong Pan,<sup>1), 2)</sup> Feiyi Liao<sup>1)</sup> and  
Yuan Lin<sup>1), 3), a)</sup>

1) *State Key Laboratory of Electronic Thin Films and Integrated Devices, University of Electronic  
Science and Technology of China, Chengdu 610054, China*

2) *Department of Civil and Environmental Engineering, Northwestern University, Evanston, IL,  
60208, USA*

3) *Institute of Electronic and information Engineering in Dongguan, University of Electronic  
Science and Technology of China, Dongguan 523808, China*

**Abstract:**

Different types of multi-walled carbon nanotubes (CNTs), synthesized by chemical vapor deposition, are used to fabricate infrared (IR) detectors on flexible substrates based on CNT  $p$ - $n$  junctions. It is found that this kind of detector is sensitive to infrared signal with power density as low as  $90 \mu\text{W}\cdot\text{mm}^{-2}$  even at room temperature. Besides, unlike other devices, the detector with this unique structure can be bended for 100 cycles without any damages and its functionality does not degenerate once it recovers to the initial state. The results give a good reference for developing efficient, low-cost, and flexible IR detectors.

a) Authors to whom correspondence should be addressed. Email: [mingao@uestc.edu.cn](mailto:mingao@uestc.edu.cn),

[linyuan@uestc.edu.cn](mailto:linyuan@uestc.edu.cn)

## Introduction

Infrared (IR) photodetectors, widely used in health care, thermal imaging, remote sensing, night vision and space observations,<sup>1-3</sup> have exhibited potential applications in wearable devices and human physical sign signal measuring devices.<sup>4-6</sup> But the wearable devices and bio-detector need to be light weight and deformable.<sup>7-10</sup> Traditional IR photodetectors are made from IV or III-V semiconductors,<sup>11, 12</sup> which are easy to be damaged or lose their efficacy after bending or stretching. To resolve this problem, Rogers's group designed serpentine structure to release the strain of traditional semiconductors at the bending state.<sup>13</sup> And there are also some researchers who are focused on some novel sensing materials with advantage of flexibility, such as graphene<sup>14, 15</sup>, two-dimensional semiconducting metal chalcogenides (2D-SMC)<sup>16-18</sup> or nanowires<sup>19-21</sup>. Carbon nanotubes (CNTs), with the well-defined one-dimensional (1D) structure and appropriate tunable band structure,<sup>22</sup> can be bended without any damage<sup>23,24</sup> and motivate the increasing interest for the application of IR detecting. There have been many studies trying to explore the use of CNTs in IR detectors.<sup>25-31</sup> At present, most of the large size CNT-based IR detectors can be divided into two categories: CNT-polymer composite films<sup>25, 32-36</sup> and suspended CNT networks,<sup>37-39</sup> which can improve the IR response of CNTs, but the fabrication of the aforementioned IR detectors is extremely complicate.

Here, we report the IR detector fabricated based on a CNT *p-n* junction formed by *n*-type CNTs and *p*-type CNTs. The detector based on this kind of structure is very sensitive even at room temperature and the IR response is obvious at light radiation with power density as low as  $90 \mu\text{W}\cdot\text{mm}^{-2}$ . Besides, after bending over 100 cycles,

the detector can still work normally. The results demonstrated that the IR detector based on this unique structure with multi-walled CNTs  $p$ - $n$  junction is feasible for the flexible sensitive devices, which has not been reported before.

### Structure and working principle of the detector

Fig. 1a is a schematic showing the structure of the detector, which consists of  $n$ -type CNTs,  $p$ -type CNTs, the silver electrodes and the flexible substrate. The voltage between the two silver electrodes is monitored and it will change when the IR is focused on the surface of the detector. The IR response of the detector mainly owes to the Thomson potential and the interface between the  $n$ -type CNTs and  $p$ -type CNTs.

Fig. 1b shows the generation of Thomson potential. When the IR radiation is focused on the  $p$ - $n$  junction of the device, temperature of the irradiated portion will increase. As the majority carrier of semiconductor is influenced by the temperature, the hot end of the  $p$ -type CNTs have much more holes than the cold side. Due to the concentration difference, the holes diffuse from the hot side to the cold side, which will produce Thomson potential between the two ends of the  $p$ -type CNTs and the cold end has a higher potential than the hot one. The same principle also works for  $n$ -type CNTs, but the hot end has a higher potential due to the different majority carrier. Thus the total Thomson potential is the superposition of both  $p$ -type CNTs and  $n$ -type CNTs for the  $p$ - $n$  junction. Moreover, enhancement in the response would be achieved due to the  $p$ - $n$  junction interface, as shown in Fig. 1c. When the  $n$ -type CNTs contacted with the  $p$ -type CNTs, electrons would flow from the  $n$ -type CNTs to the  $p$ -type CNTs. Thus the surface of the  $n$ -type CNTs presents positive electricity and the surface of the  $p$ -type

CNTs presents negative electricity, which raises the electric potential of the *n*-type CNTs and lowers the electric potential of the *p*-type CNTs at the same time. An inner electric field appears at the interface between the CNT *p-n* junction and the electric field points from *n*-type CNTs to *p*-type CNTs. When the IR is focused on the surface of the detector, photogenic charge carriers and hot charge carriers will occur. Under the action of the inner electric field, the carriers will move directionally: holes will flow to the *p*-type CNTs and electrons will flow to the *n*-type CNTs, as shown in Fig. 1c. As a result, the potential of the *p*-type CNTs will increase with the IR radiation and the potential of the *n*-type CNTs will decrease at the same time. Thus the change of the voltage between the two electrodes can be detected.

#### **Fabrication of the detector**

The floating catalyst chemical vapor deposition (CVD) method<sup>40-42</sup> was used to synthesize both non-doped CNTs and nitrogen doped CNTs (NCNTs). Schematic of the equipment and process flow can be seen in supporting information S1. Technically, a silicon substrate with a 300-nm-thick SiO<sub>2</sub> layer was put in the quartz tube as a holder. Then the quartz tube was heated to 800 °C and precursor solution was introduced in the quartz tube by an injector. When the growth began, a forming gas (3 % H<sub>2</sub>+ 97% argon) was used as the carrier gas to transfer the carbon source and catalyst into the middle of the quartz tube. To get different types of CNTs, we can control the concentration of precursor solution and the growth conditions. For non-doped CNTs, the precursor solution is 2 wt % ferrocene in cyclohexane, and the precursor solution was preheated to 200 °C with an injection speed of 8 mL/h. On the

other hand, for NCNTs, the precursor solution is 2 wt % ferrocene in the mixture of acetonitrile and ethanol (4:1 wt), and the precursor solution was preheated to 250 °C with an injection speed of 8mL/h. The non-doped multi-walled CNTs tend to present *p*-type semiconductor properties due to some defects existing in the material.<sup>43, 44</sup> With the doping of nitrogen element, the NCNTs present *n*-type semiconductor properties due to the one more electron on the nitrogen atom than carbon.

Fig. 2a shows the fabrication procedures for the flexible IR detector based on the CNT *p-n* junction. The NCNT arrays were chosen as the *n*-type material and non-doped CNT arrays were chosen as the *p*-type material. First, a strip of PMMA tape was pressed on the surface of the NCNT arrays and then the NCNT arrays were stuck on the tape and peeled off from the SiO<sub>2</sub> substrate. Second, this strip of tape was put on the non-doped CNT arrays and peeled them off similarly. It is worth noting that the two types of CNT arrays overlap each other in the central part of the tape. As shown in Fig. 2a, the size of the overlap is 3 mm × 3 mm. This area is used as the sensitive part in the detector. Fig. 2b shows the optical photograph of the detector. It is clear that the detector can be bent in any angle. Fig. 2c shows the section morphology of the detector. Three different places of the detector (labeled as 1, 2 and 3 in Fig. 2a, respectively) are presented on the SEM. From the image, we know the thickness of the CNT arrays is about 121.9 μm in place 1 and 112 μm in place 3. The place 2 shows the overlap of the CNTs and NCNTs. The top is non-doped CNTs and the bottom is NCNTs. The thicknesses of non-doped CNTs and NCNTs are about 94μm and 108.6μm in this overlap place, respectively. Both of the thicknesses are a little

thinner than those in the non-overlap place for the reason that the CNT arrays and NCNT arrays cross each other at this place. The cross of the CNTs and NCNTs strengthens the interface areas, which build the *p-n* junction. Fig. 2d shows the details of the non-doped CNT arrays and the inset image shows the diameter of the CNT is about 35.3 nm. Fig. 2e shows the details of the NCNT arrays and the inset image shows the diameter of the NCNT is about 50.1 nm. From the X-ray photoelectron spectroscopy of CNTs (N1s spectrum) shown in Fig 2f, we know that the nitrogen has been doped into the CNTs successfully. The existence of three nitrogen element components can be fitted by three peaks which centered at 398.3 eV, 401.1 eV and 404.7 eV, respectively. Peaks at 398.3 eV and 401.1 eV are pyridine-like nitrogen and graphite-like nitrogen, respectively.<sup>45, 46</sup> The peak at 404.7 eV owes to the molecular N<sub>2</sub> intercalated at the carbon walls or trapped in the compartments. Moreover, Raman spectra of both CNTs and NCNTs have been tested (shown in supporting information S2), which can also give the powerful evidence that the nitrogen have been doped into the structure of NCNTs successfully. Then we fabricated field effect transistor (FET) devices with these two kinds of multi-walled CNTs and the performance of the FET devices proved that the as-prepared undoped CNTs present p-type semiconductor property and the as-prepared nitrogen-doped CNTs (NCNTs) present *n*-type semiconductor property (shown in supporting information S3). Both CNTs and NCNTs demonstrated photo absorption in the wavelength from 260 nm to 7000 nm, as shown in supporting information S4. At last, for comparison, detectors with CNTs only or NCNTs only were also made. The strips of PMMA tapes were pressed on the

surfaces of the corresponding arrays and then the arrays were stuck on the tapes and peeled off from the SiO<sub>2</sub> substrates.

## Results and discussion

The current-voltage characteristic of the *p-n* junction device under dark and IR illumination are shown in Fig. 3, measured at room temperature in the air. The I-V curve is linear with the resistance of 8 kΩ, indicating there is no rectification characteristic despite the *p-n* junction structure of the device. This phenomenon owes to the CVD-grown multi-walled CNTs, which consist of both the semiconductive and metallic CNTs.<sup>47</sup> The metallic CNTs will influence the I-V curve of the device and the detailed reason is shown in supporting information S5. The performance of the as-prepared multi-walled based FET devices shown in supporting information S3 demonstrates relatively large drain-source currents at the off-state of the FET devices, indicating that both as-prepared CNTs and NCNTs contain the metallic CNTs. Remarkably, despite the absence of rectification, the I-V curve of the device shifts downward, generating a larger open circuit photovoltage  $V_{oc}$  at zero current and a larger net photocurrent at zero bias, as shown in Fig. 3 (red line). Besides, there is already a open voltage even when the IR is off, which is due to the thermal radiation from the environment and we will give a detailed discussion below in Fig. 5a.

Fig. 4a, 4c and 4e show the IR response upon the on/off infrared laser for the three kinds of structure: *p*-type (CNTs) only, *n*-type (NCNTs) only and the *p-n* junction. The power density of IR radiation is 0.32 mW·mm<sup>-2</sup> and the wavelength of the light is 850 nm. The experiments were carried out in the air at room temperature

(about 25 °C). Fig. 4b, 4d and 4f schematically show the structures of the detectors. For detector based on *p*-type only or *n*-type only, the IR radiation was focused on the silver electrode (thickness is about 100 μm). If the IR was focused on the center of the only *p*-type or *n*-type CNT based detector, there will be no response for the symmetrical structure, as shown in supporting information S6. For detector based on the *p-n* junction, the IR was focused on the overlap areas of the *n*-type and *p*-type CNTs. As shown in Fig. 4a, for detector based on *p*-type only, when the IR was turned on, the voltage decreased (from 0 μV to -14 μV). Yet, for detector based on *n*-type only, the voltage increased (from 0 μV to 9 μV) upon the IR radiation, as shown in Fig. 4c. The opposite results owe to the different type of the semiconductor properties for the two types of CNTs and these results also proved that the doping of nitrogen had changed the properties of the CNTs successfully. Fig. 4e shows the IR response for detector based on *p-n* junction. It can be seen the voltage increased from 11 μV to 36 μV upon the IR radiation. The voltage response to the on-off IR radiation shows exponential rise and fall behaviors (supporting information S7). The response time of the device taken at 80% magnitude change is 7.5 s and the recovery time is 8.8 s. The longer response/recovery time compared with other reported work is highly possibly due to factors such as a large exposure area and low thermal conductivity of the PMMA substrate (0.18 W/(m·K)). Usually, a larger exposure/sense area makes the sensor more sensitive, but also makes the sensor have a longer response time.<sup>37</sup> The amplitude of the response is about 25 μV, which is bigger than the other two kinds of detectors. Because the *p-n* junction based device not only possesses the superimposed

effect of both *n*-type CNTs and *p*-type CNT, but also has the enhancement effect from the *p-n* contacting interface, as discussed above. Besides, the structures of the detectors based on *p*-type or *n*-type only CNT are symmetrical, which means no response will be monitored if the IR radiation focuses on the whole detector. But the detector based on *p-n* junction can work normally in this situation for its asymmetric structure, thus it's more practical in our daily life.

For the detector based on *p-n* junction, as shown in Fig. 3 (black line) and Fig. 4e, even if there is no IR radiation, the monitored voltage is not zero, which is quite different from the other two symmetrical structures. The nonzero original voltage may owe to the thermal radiation from the surrounding environment and adsorbed gas from the air. Fig. 5a shows the changes of the original voltage  $V_0$  with temperature. When the detector was put in vacuum (about 0.01 Pa),  $V_0$  increased from 11  $\mu\text{V}$  to about 29  $\mu\text{V}$  for the release of the adsorbed gas in air (such as oxygen). With the decrease of the temperature from 300 K to 90 K, original voltage  $V_0$  increased from 29  $\mu\text{V}$  to 144  $\mu\text{V}$ . That is because when the temperature decreases, band gap of both the *n*-type and *p*-type CNTs increases, which leads to the increase of barrier between these two kinds of CNTs. The higher barrier means a bigger built-in electric field. As discussed above, electric carriers will move directionally under the action of built-in electric field, which generates the open voltage. Thus with a bigger built-in electric field, there will be a higher original voltage (open voltage). The dependence of the response on the incident IR power density is shown in Fig. 5b and 5c. Fig. 5b shows the IR response at the IR power density of 0.4, 0.29, 0.2 and 0.09  $\text{mW}\cdot\text{mm}^{-2}$ . The

response amplitude decreased from 30  $\mu\text{V}$  at  $0.4 \text{ mW}\cdot\text{mm}^{-2}$  to 6.5  $\mu\text{V}$  at  $0.09 \text{ mW}\cdot\text{mm}^{-2}$ . Results indicated that detectors based on this structure are sensitive even under a very lower IR power density (as low as  $0.09 \text{ mW}\cdot\text{mm}^{-2}$ ) at room temperature. Fig. 5c shows the changes of the response amplitude and responsivity with different IR power density for the detector based on CNT *p-n* junction. It's clear that the response amplitude shows a linear relationship with the IR power density. The value of responsivity with different IR power density is similar and we use a horizontal line to fit these data. The average responsivity is about  $1.05\times 10^{-2} \text{ V/W}$ , corresponding to a noise equivalent power of  $5.7\times 10^{-5} \text{ W}$ , and a special detectivity of  $1.289\times 10^3 \text{ cm Hz}^{1/2} \text{ W}^{-1}$  (at low frequency 0.02 Hz). The method to calculate the responsivity and detectivity of the detector is shown in supporting information S8. To examine the switching behavior of the detector in more detail, pulsed IR signals with various time periods were used with the IR power density of  $0.32 \text{ mW}\cdot\text{mm}^{-2}$ , as shown in Fig. 5d. When the period of the pulsed IR signal increases from 5 s (supporting information S9) to 50 s, difference between the peak and valley of the voltage wave becomes larger, as shown in Fig. 5e. A plot of the IR response amplitude as a function of pulse period, shown in Fig. 5f, clearly indicates that the response of the detector tends to be more obvious with longer IR pulse period. Inset of Fig. 5f shows the linear relationship between the IR response amplitude and the log scale IR pulse period. Besides, the responsivity of the detector versus the period of IR pulse was also calculated and the results are shown in supporting information S10.

To explore the performance of the detector at the state of bending, the IR response at different bending angle has been tested. Fig. 6a shows the response at the period on/off IR radiation at different bending angle and the power density is  $0.36 \text{ mW}\cdot\text{mm}^{-2}$ . Fig. 6b shows the linear relationship between the response amplitude and the light power density at different bending angle. And the inset of Fig. 6b shows the decrease of responsivity with the increase of bending angle. I is the state of the detector without bending. II is the state when the height of the bending arch is up to 2 mm. III is the state when the height of the bending arch is 4 mm. IV means the detector recovers to the initial state after 100 cycles of bending. It can be seen that the IR response amplitude decreased from about  $27 \mu\text{V}$  to  $16 \mu\text{V}$ , or responsivity decreased from  $1.05\times 10^{-2} \text{ V/W}$  to  $0.55\times 10^{-2} \text{ V/W}$  with the height of the bending arch increases from 0 to 4 mm. However, when the detector recovered from the bending state, the response also returned to the original amplitude (IV). That means the bending of the detector would weaken the sensitivity. But the detector was not damaged by the bending and it could work normally as soon as it recovered to the initial state. Fig. 6c shows the strain simulation for the bending of the IR detector and Fig. 6d shows the details of the section view. The strain of the sensitive film (CNT arrays) becomes larger with the increase of the bending, which means the space between the adjacent CNT (indicated as  $x$  in Fig. 6e) increases with the bending. The response of the IR detector is dependent on the interface between the CNTs  $p$ - $n$  junction and the increase of the distance between adjacent CNTs will weaken the role

of the interface. Thus the response will decrease with the increase of the bending, as shown in Fig. 6a and 6b.

### Conclusions

In summary, flexible IR detectors based on CNT *p-n* junctions have been fabricated. The CNT *p-n* junction was constructed by two types of multi-walled CNT arrays, which were grown by the CVD method. This detector is sensitive and the response is obvious under a weak IR radiation with the power density as low as  $90 \mu\text{W}\cdot\text{mm}^{-2}$ . Besides, with the unique vertical array structure, the detector can be bended without any damage and can work normally after recovery. The proposed design is an ideal candidate for the flexible IR detector, which is sensitive and low-cost.

### Acknowledgements

This work is supported by the National Basic Research Program of China (973 Program) under Grant No. 2015CB351905, the National Natural Science Foundation of China (Nos. 11329402 and 61306015), the Technology Innovative Research Team of Sichuan Province of China (No. 2015TD0005), “111” project (No.B13042) and Guangdong Innovative Research Team Program (No. 201001D0104713329).

## References

1. T. Rauch, M. Boberl, S. F. Tedde, J. Furst, M. V. Kovalenko, G. Hesser, U. Lemmer, W. Heiss and O. Hayden, *Nat. Photon.*, 2009, **3**, 332-336.
2. R. Schodel, T. Ott, R. Genzel, R. Hofmann, M. Lehnert, A. Eckart, N. Mouawad, T. Alexander, M. J. Reid, R. Lenzen, M. Hartung, F. Lacombe, D. Rouan, E. Gendron, G. Rousset, A. M. Lagrange, W. Brandner, N. Ageorges, C. Lidman, A. F. M. Moorwood, J. Spyromilio, N. Hubin and K. M. Menten, *Nature*, 2002, **419**, 694-696.
3. X. Qian, L. Han, Y. Wang and B. Wang, *Infrared Phys. Technol.*, 2013, **57**, 36-41.
4. K. Malhi, S. C. Mukhopadhyay, J. Schnepfer, M. Haefke and H. Ewald, *Sensors Journal, IEEE*, 2012, **12**, 423-430.
5. R. A. Cernat, C. Ungureanu, G. M. Ungureanu, R. Aarts and J. Arends, 2014.
6. L. Gao, D. Dong, J. He, K. Qiao, F. Cao, M. Li, H. Liu, Y. Cheng, J. Tang and H. Song, *Appl. Phys. Lett.*, 2014, **105**, 153702.
7. W.-H. Yeo, Y.-S. Kim, J. Lee, A. Ameen, L. Shi, M. Li, S. Wang, R. Ma, S. H. Jin, Z. Kang, Y. Huang and J. A. Rogers, *Adv. Mater.*, 2013, **25**, 2773-2778.
8. S. Yao and Y. Zhu, *Nanoscale*, 2014, **6**, 2345-2352.
9. J. Kim, A. Banks, H. Cheng, Z. Xie, S. Xu, K. I. Jang, J. W. Lee, Z. Liu, P. Gutruf and X. Huang, *Small*, 2015, **11**, 906-912.
10. Y. Tai, M. Mülle, I. Aguilar Ventura and G. Lubineau, *Nanoscale*, 2015, **7**, 14766-14773.

11. F.-S. Juang, Y.-K. Su, H. H. Yu and K.-J. Liu, *Mater. Chem. Phys.*, 2003, **78**, 620-624.
12. A. Rogalski, *Prog. Quantum Electronics*, 2003, **27**, 59-210.
13. Y. M. Song, Y. Xie, V. Malyarchuk, J. Xiao, I. Jung, K.-J. Choi, Z. Liu, H. Park, C. Lu, R.-H. Kim, R. Li, K. B. Crozier, Y. Huang and J. A. Rogers, *Nature*, 2013, **497**, 95-99.
14. T. Q. Trung, S. Ramasundaram and N.-E. Lee, *Adv. Funct. Mater.*, 2015, **25**, 1745-1754.
15. N. Liu, H. Tian, G. Schwartz, J. B.-H. Tok, T.-L. Ren and Z. Bao, *Nano Lett.*, 2014, **14**, 3702-3708.
16. G. H. Chen, Y. Q. Yu, K. Zheng, T. Ding, W. L. Wang, Y. Jiang and Q. Yang, *Small*, 2015, **11**, 2848-2855.
17. Z. Wang, M. Safdar, M. Mirza, K. Xu, Q. Wang, Y. Huang, F. Wang, X. Zhan and J. He, *Nanoscale*, 2015, **7**, 7252-7258.
18. D. B. Velusamy, R. H. Kim, S. Cha, J. Huh, R. Khazaeinezhad, S. H. Kassani, G. Song, S. M. Cho, S. H. Cho, I. Hwang, J. Lee, K. Oh, H. Choi and C. Park, *Nat. Commun.*, 2015, **6**, 8063.
19. Yoo, S. Jeong, S. Kim and J. H. Je, *Adv. Mater.*, 2015, **27**, 1712-1717.
20. W. Deng, X. Zhang, L. Huang, X. Xu, L. Wang, J. Wang, Q. Shang, S. T. Lee and J. Jie, *Adv. Mater.*, 2016, doi: 10.1002/adma.201505126.
21. C. Yan, J. Wang, X. Wang, W. Kang, M. Cui, C. Y. Foo and P. S. Lee, *Adv. Mater.* 2014, **26**, 943-950.

22. T. W. Odom, J.-L. Huang, P. Kim and C. M. Lieber, *Nature*, 1998, **391**, 62-64.
23. R. Saito, G. Dresselhaus and M. S. Dresselhaus, *Physical properties of carbon nanotubes*, World Scientific, 1998.
24. S. Xie, W. Li, Z. Pan, B. Chang and L. Sun, *J. Phys. Chem. Solids*, 2000, **61**, 1153-1158.
25. I. Hwang, H. J. Jung, S. H. Cho, S. S. Jo, Y. S. Choi, J. H. Sung, J. H. Choi, M. H. Jo and C. Park, *Small*, 2014, **10**, 653-659.
26. R. Lu, C. Christianson, A. Kirkemide, S. Ren and J. Wu, *Nano Lett.*, 2012, **12**, 6244-6249.
27. Y. Liu, N. Wei, Q. Zhao, D. Zhang, S. Wang and L.-M. Peng, *Nanoscale*, 2015, **7**, 6805-6812.
28. C. Xie, B. Nie, L. Zeng, F.-X. Liang, M.-Z. Wang, L. Luo, M. Feng, Y. Yu, C.-Y. Wu and Y. Wu, *ACS nano*, 2014, **8**, 4015-4022.
29. Y. L. Kim, H. Y. Jung, S. Park, B. Li, F. Liu, J. Hao, Y.-K. Kwon, Y. J. Jung and S. Kar, *Nat. Photonics*, 2014, **8**, 239-243.
30. W. Niu, L. T. Su, R. Chen, H. Chen, Y. Wang, A. Palaniappan, H. Sun and A. I. Yoong Tok, *Nanoscale*, 2014, **6**, 817-824.
31. S. Park, S. J. Kim, J. H. Nam, G. Pitner, T. H. Lee, A. L. Ayzner, H. Wang, S. W. Fong, M. Vosgueritchian and Y. J. Park, *Adv. Mater.*, 2015, **27**, 759-765.
32. B. Pradhan, R. R. Kohlmeier, K. Setyowati, H. A. Owen and J. Chen, *Carbon*, 2009, **47**, 1686-1692.
33. B. Pradhan, K. Setyowati, H. Liu, D. H. Waldeck and J. Chen, *Nano Lett.*,

- 2008, **8**, 1142-1146.
34. D. Bang, J. Lee, J. Park, J. Choi, Y. W. Chang, K.-H. Yoo, Y.-M. Huh and S. Haam, *J. Mater. Chem.*, 2012, **22**, 3215-3219.
35. A. E. Aliev, *Infrared Phys. Technol.*, 2008, **51**, 541-545.
36. G. E. Fernandes, J. H. Kim, A. K. Sood and J. Xu, *Adv. Funct. Mater.*, 2013, **23**, 4678-4683.
37. J. John, M. Muthee, M. Yogeesh, S. K. Yngvesson and K. R. Carter, *Adv. Opt. Mater.*, 2014, **2**, 581-587.
38. R. Lu, Z. Li, G. Xu and J. Z. Wu, *Appl. Phys. Lett.*, 2009, **94**, 163110.
39. M. E. Itkis, F. Borondics, A. Yu and R. C. Haddon, *Science*, 2006, **312**, 413-416.
40. X. Li, A. Cao, Y. J. Jung, R. Vajtai and P. M. Ajayan, *Nano Lett.*, 2005, **5**, 1997-2000.
41. S. Talapatra, S. Kar, S. Pal, R. Vajtai, L. Ci, P. Victor, M. Shaijumon, S. Kaur, O. Nalamasu and P. Ajayan, *Nat. Nanotechnol.*, 2006, **1**, 112-116.
42. S. Liu, Y. Zhang, Y. Lin, Z. Zhao and Q. Li, *Carbon*, 2014, **69**, 247-254.
43. Z. Li, V. P. Kunets, V. Saini, Y. Xu, E. Dervishi, G. J. Salamo, A. R. Biris and A. S. Biris, *ACS nano*, 2009, **3**, 1407-1414.
44. V. Derycke, R. Martel, J. Appenzeller and P. Avouris, *Appl. Phys. Lett.*, 2002, **80**, 2773-2775.
45. H. Liu, Y. Zhang, R. Li, X. Sun, S. Désilets, H. Abou-Rachid, M. Jaidann and L.-S. Lussier, *Carbon*, 2010, **48**, 1498-1507.

46. X. Tao, X. Zhang, F. Sun, J. Cheng, F. Liu and Z. Luo, *Diamond Relat. Mater.*, 2007, **16**, 425-430.
47. X. He, N. Fujimura, J. Lloyd, K. J. Erickson, A. A. Talin, Q. Zhang, W. Gao, Q. Jiang, Y. Kawano, R. H. Hauge and F. Léonard, *Nano Lett.*, 2014, **14**, 3953-3958.

**Figures Captions:**

**Fig. 1** (a) Schematic illustration of the detector's structure. (b) and (c) Working principle of the IR detector based on CNT  $p-n$  junction. (b) Thomson potential owes to the carrier diffusion for the temperature difference. (c) Carriers move directionally under the action of the  $p-n$  junction build-in electric field.

**Fig. 2** (a) Schematic illustration of the fabrication procedures for the flexible IR detector based on CNT  $p-n$  junction. The non-doped CNTs present  $p$ -type semiconductor and the nitrogen doped CNTs (NCNTs) present  $n$ -type semiconductor. (b) The optical photograph of the IR detector. (c) The section morphology of the detector. Place 1 shows the thickness of the NCNTs ( $n$ -type CNTs), place 3 shows the thickness of the CNTs ( $p$ -type CNTs) and place 2 shows the overlap of the CNTs and NCNTs. (d) The section morphology of the CNT arrays. The inset shows the diameter of CNT. (e) The section morphology of NCNTs arrays. The inset shows the diameter of NCNTs. (f) The X-ray photoelectron spectroscopy of NCNTs (N1s spectrum).

**Fig. 3** I-V curve of the multi-walled CNTs  $p-n$  junction based detector in the dark and under IR illumination.

**Fig. 4** IR response for the detectors of CNTs ( $p$ -type), NCNTs ( $n$ -type) and CNT  $p-n$  junction. (a) The IR response for CNTs. (c) The IR response for NCNTs. (e) The IR response for CNT  $p-n$  junction. (b), (d) and (f) show the testing schematic diagrams for the detectors.

**Fig. 5** (a) The original value of the voltage  $V_0$  for the detector with different temperature. (b) The response of the detector at the on/off IR radiation with different power density. (c) The response amplitude and responsivity of the detector versus the IR power density. (d) Schematic diagram of the periodic on/off IR radiation. (e) Response of the detector at the on/off radiation with different IR on-off period. (f) Response amplitude of the detector as a function of IR on-off period. Inset shows the response amplitude as a function of log scale IR on-off period.

**Fig. 6** The performance of the IR detector after bending. (a) The response of the detector at the on/off IR radiation with different levels of bending. (b) The linear relationship for the response amplitude and the light power density with different bending angle. The inset shows the decreasing of responsivity with the increasing of bending angle. (c) Strain simulation for the IR detector with different levels of bending. I shows the strain state without bending. II shows the strain state when the height of the bending arch is up to 2 mm. III shows the strain state when the height of the bending arch is up to 4 mm. IV shows the strain state when the IR detector is recover to the initial condition ( $h = 0$  mm) after over 100 cycles of bending. (d) The section view of strain state for the detector materials (CNT arrays). I, II and III are as shown in (c). (e) Schematic illustration of the CNT arrays' state after bending.  $x$  is the distance between the adjacent CNTs.

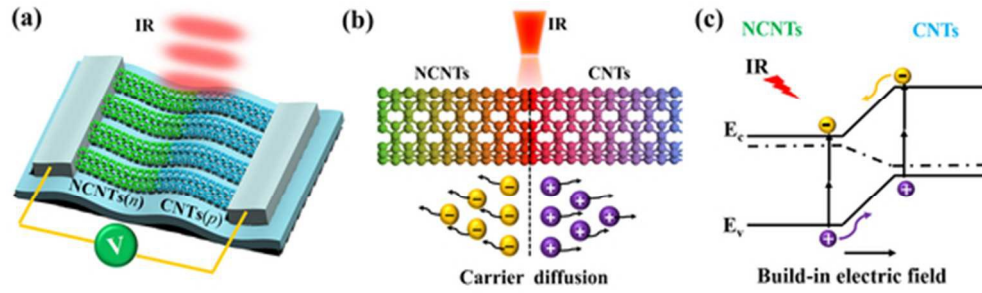


**Fig. 1** (a) Schematic illustration of the detector's structure. (b) and (c) Working principle of the IR detector based on CNT  $p$ - $n$  junction. (b) Thomson potential owes to the carrier diffusion for the temperature difference. (c) Carriers move directionally under the action of the  $p$ - $n$  junction build-in electric field.  
49x14mm (300 x 300 DPI)

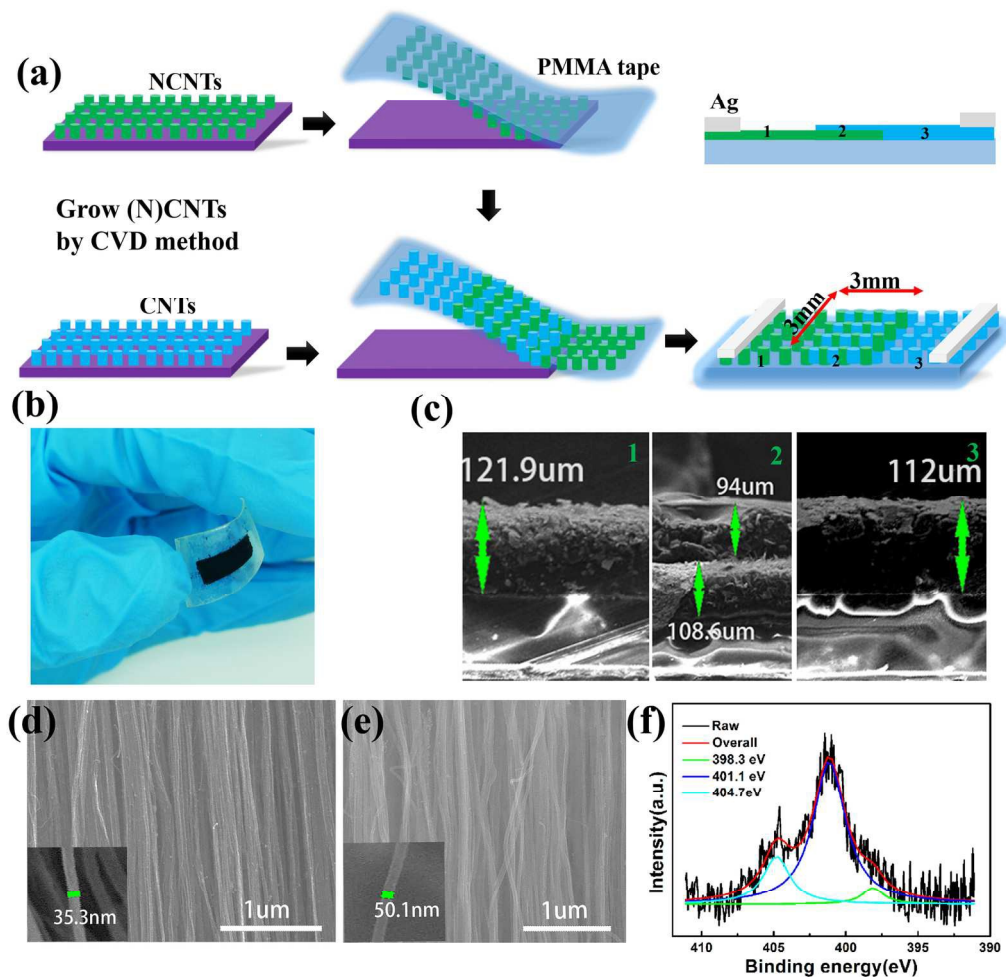


**Fig. 2** (a) Schematic illustration of the fabrication procedures for the flexible IR detector based on CNT  $p$ - $n$  junction. The non-doped CNTs present  $p$ -type semiconductor and the nitrogen doped CNTs (NCNTs) present  $n$ -type semiconductor. (b) The optical photograph of the IR detector. (c) The section morphology of the detector. Place 1 shows the thickness of the NCNTs ( $n$ -type CNTs), place 3 shows the thickness of the CNTs ( $p$ -type CNTs) and place 2 shows the overlap of the CNTs and NCNTs. (d) The section morphology of the CNT arrays. The inset shows the diameter of CNT. (e) The section morphology of NCNTs arrays. The inset shows the diameter of NCNTs. (f) The X-ray photoelectron spectroscopy of NCNTs (N1s spectrum). 167x165mm (300 x 300 DPI)

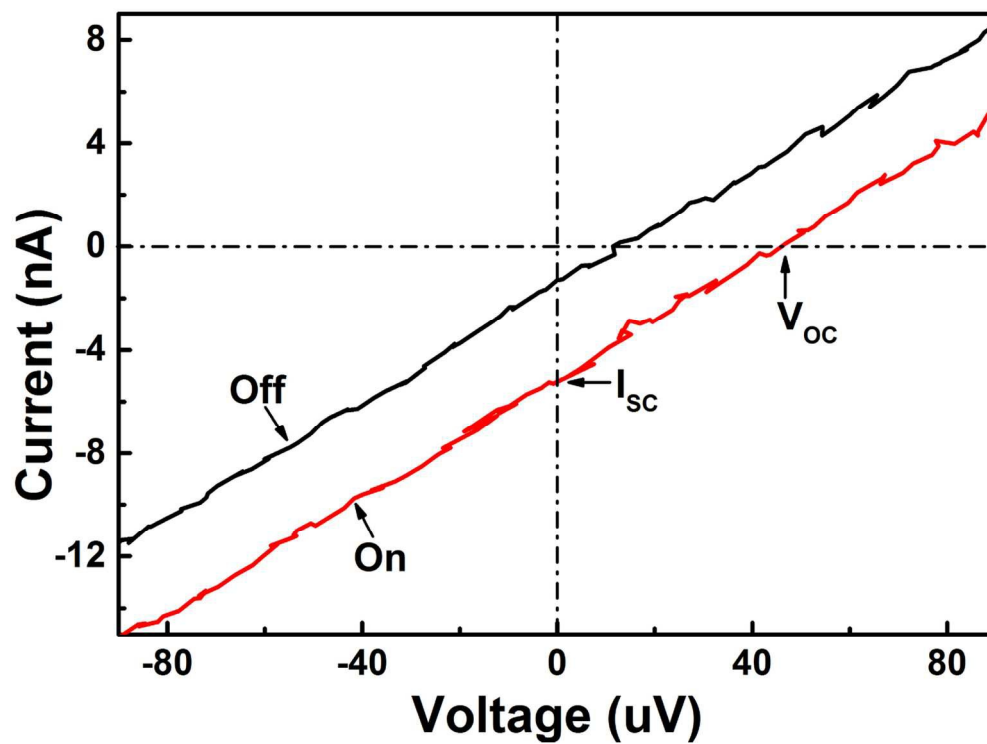


**Fig. 3** I-V curve of the multi-walled CNTs *p-n* junction based detector in the dark and under IR illumination. 125x92mm (300 x 300 DPI)

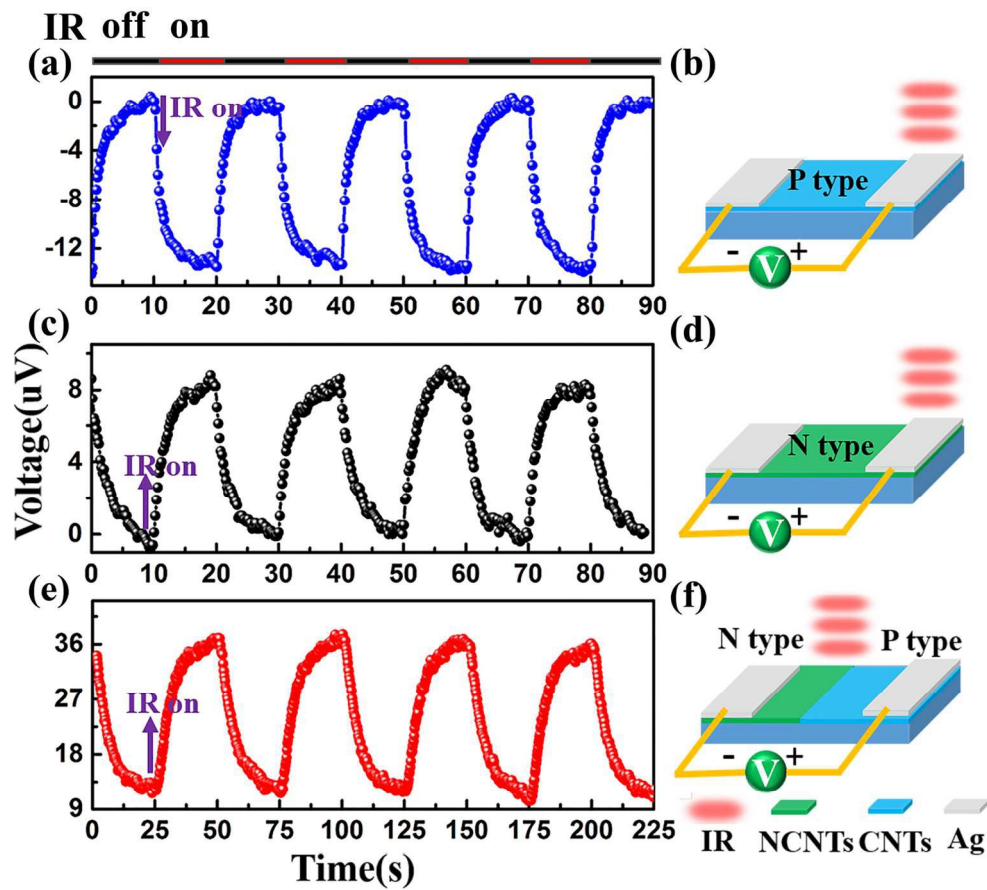


**Fig. 4** IR response for the detectors of CNTs (*p*-type), NCNTs (*n*-type) and CNT *p-n* junction. (a) The IR response for CNTs. (c) The IR response for NCNTs. (e) The IR response for CNT *p-n* junction. (b), (d) and (f) show the testing schematic diagrams for the detectors.  
149x131mm (300 x 300 DPI)

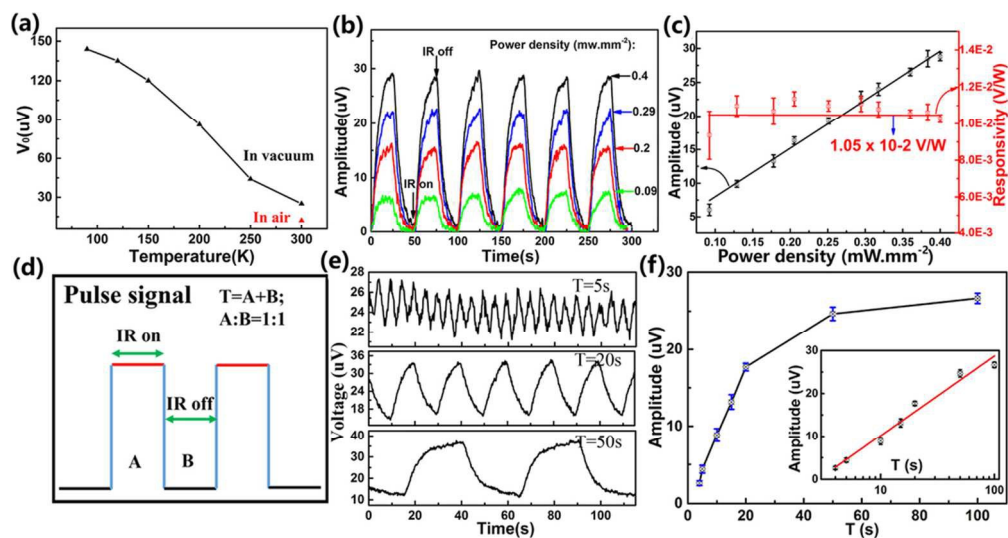


**Fig. 5** (a) The original value of the voltage  $V_0$  for the detector with different temperature. (b) The response of the detector at the on/off IR radiation with different power density. (c) The response amplitude and responsivity of the detector versus the IR power density. (d) Schematic diagram of the periodic on/off IR radiation. (e) Response of the detector at the on/off radiation with different IR on-off period. (f) Response amplitude of the detector as a function of IR on-off period. Inset shows the response amplitude as a function of log scale IR on-off period.  
90x48mm (300 x 300 DPI)

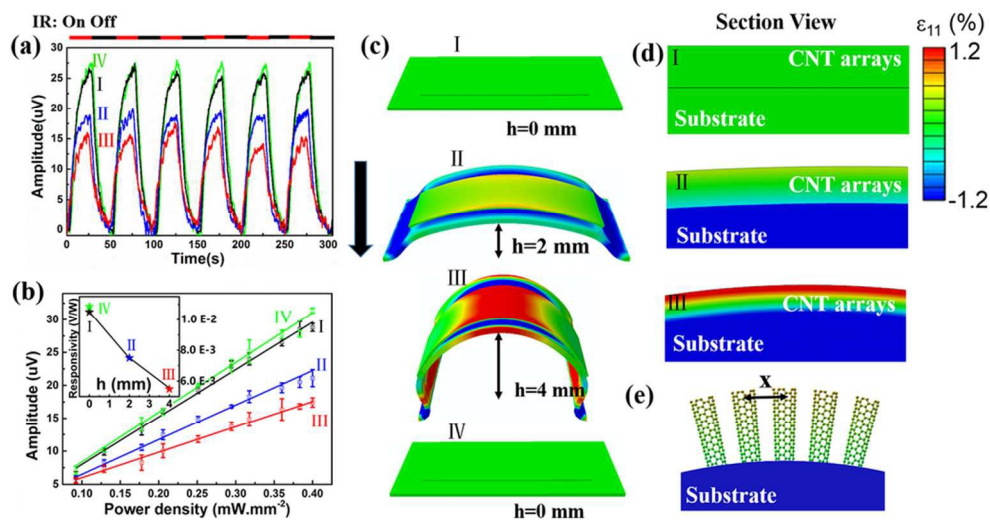


**Fig. 6** The performance of the IR detector after bending. (a) The response of the detector at the on/off IR radiation with different levels of bending. (b) The linear relationship for the response amplitude and the light power density with different bending angle. The inset shows the decreasing of responsivity with the increasing of bending angle. (c) Strain simulation for the IR detector with different levels of bending. I shows the strain state without bending. II shows the strain state when the height of the bending arch is up to 2 mm. III shows the strain state when the height of the bending arch is up to 4 mm. IV shows the strain state when the IR detector is recover to the initial condition ( $h = 0$  mm) after over 100 cycles of bending. (d) The section view of strain state for the detector materials (CNT arrays). I, II and III are as shown in (c). (e) Schematic illustration of the CNT arrays' state after bending.  $x$  is the distance between the adjacent CNTs.

89x46mm (300 x 300 DPI)